Electroless Production of Fertilizer (Struvite) and Hydrogen from Synthetic Agricultural Wastewaters

László Kékedy-Nagy[a#], Mojtaba Abolhassani[a#], Sergio I. Perez Bakovic[a], Zahra Anari[a], John P. Moore II[a], Bruno G. Pollet[b] and Lauren F. Greenlee[a]*

[a]Ralph E. Martin Department of Chemical Engineering, University of Arkansas, 3202 Bell Engineering Center, Fayetteville, Arkansas 72701, United States

[b]Hydrogen Energy and Sonochemistry research group, Department of Energy and Process Engineering, Faculty of Engineering, Norwegian University of Science and Technology (NTNU), NO-7491 Trondheim, Norway

*Corresponding author: Tel.: 610-507-6390, E-mail: greenlee@uark.edu

[#]Contributed equally to this work.

ABSTRACT

The drive towards sustainable phosphorous (P) recovery from agricultural and municipal wastewater streams has intensified. However, combining P recovery with energy conservation is perhaps one of the greatest challenges of this century. In this study, we report for the first time, the simultaneous electroless production of struvite and di-hydrogen from aqueous ammonium dihydrogen phosphate ($NH_4H_2PO_4$) solutions in contact with either a pure magnesium (Mg) or a Mg alloy as the anode and 316 stainless steel (SS) as the cathode placed in a bench-scale electrochemical reactor. During the electroless process (i.e., in the absence of external electrical power), the open circuit potential (OCP), the formation of struvite on the anode, and the generation of di-hydrogen at the cathode were monitored. We found that struvite is formed, and that struvite crystal structure/morphology and precipitate film thickness are affected by the concentration of the $H_nPO_4^{n-3}/NH_4^+$ in solution and the composition of the anode. The pure Mg anode produced a porous, 0.6-4.1 µm thick film, while the AZ31 Mg alloy produced a more compact, 1.7-9.9 µm thick struvite film. Kinetic analyses revealed that Mg dissolution to Mg^{2+} followed mostly a zero-order kinetic rate law for both Mg anode materials and the rate constants (k) depended upon the struvite layer morphology. Fourier-transform infrared spectrometry (FT-IR), X-ray diffraction (XRD), and scanning electron microscopy (SEM) indicated that the synthesized struvite was of high quality. The di-hydrogen and Mg^{2+} in solution were detected by a gas chromatography (GC)-thermal conductivity detector (TCD) and ion chromatography (IC), respectively. Furthermore, we fully demonstrate that the reactor was able to remove ~73% of the $H_nPO_4^{n-3}$ present in a natural poultry wastewater as mainly struvite. This study highlights the feasability of simultaneously producing struvite and di-hydrogen from wastewater effluents with no energy input in a green and sustainable approach.

Keywords. Electrochemistry, open circuit potential, struvite, magnesium, sacrificial anode.

1. INTRODUCTION

Rapid population growth over the years has led to agricultural and municipal intensification and urbanization, yielding a variety of water quality problems on a global scale.[1-3] Agro-industrial wastewaters contain high levels of nutrients like phosphorus (P) or nitrogen (N), and it is estimated that 50-80% of these nutrients are lost.[4] The values of P being discharged in wastewater streams vary based upon their source of origin, and thus can range from 8.5 mg/L in landfill leachate to 740 mg/L in fresh urine.[5-6] Moreover, P is a non-renewable resource, and its geographic concentration as minable phosphate rock creates political/economic risks for the vast majority of countries.[7] As a result of these circumstances, the recycling of P from wastewater effluents, as a renewable source to sustain the high global P demand, has become a dominant goal.[8-9]

One beneficial approach to P recovery from wastewater is through struvite crystallization.[10] Magnesium ammonium phosphate hexahydrate ($MgNH_4PO_4*6H_2O$), commonly known as struvite or MAP, is a white, orthorhombic, poorly soluble crystal. Struvite is considered as a premium grade slow-release fertilizer and, thus, is an economically viable product in agriculture.[11-12] The crystallization of struvite depends upon supersaturation, the presence of impurities in solution, pH, and temperature. The general reaction may be expressed as follows:

$$Mg^{2+} + NH_4^+ + H_nPO_4^{n-3} + 6H_2O \rightarrow MgNH_4PO_4 * 6H_2O \downarrow + nH^+ \quad (1)$$

where n = 0, 1 or 2 and is based upon the solution pH.[13-15] The primary method to obtain struvite is by chemical precipitation, where extra chemicals (i.e., various magnesium salts and base) are added into the water to supply Mg and adjust the pH.[16-20] One promising technology for struvite recovery is by using microbial fuel cells (MFCs), while producing electricity simultaneously.[21-22]

On the other hand, electrochemical precipitation[23-27] and electrocoagulation processes[15, 28-32] have gained significant interest in recent years, by offering a new and exciting approach for struvite

crystallization as a feasible alternative to chemical dosage.[33] In this approach, an electrolysis cell similar to the cell depicted in Figure 1 is generally employed, in which Mg or a Mg alloy is used as the sacrificial anode. The dissolution of the anode (oxidation) provides the required amount of Mg in the form of Mg^{2+} cations for struvite precipitation.[24, 26-27, 34] According to Song *et al.*,[35] the formation of Mg^{2+} involves a two-step process, as shown in Scheme 1. In the first step, Mg is oxidized into monovalent Mg^{+} ions (an unstable intermediate), while in the second step, the intermediate Mg^{+} species are further oxidized to Mg^{2+} ions in solution, thus generating di-hydrogen (H_2) in the process. Concomitantly at the cathode, hydroxide anions (OH^-) and H_2 are produced through the oxygen reduction (ORR) and hydrogen evolution (HER) reactions in the pH range of 7.5-9.3, leading to an increase in the pH in the immediate vicinity of the cathode (Scheme 1).[23, 26, 36] Typically, during the electrochemical precipitation of struvite, a significant overpotential (η) is used to drive the reaction, implying that the electrochemical cell needs more energy than thermodynamically expected to drive the reactions. In other words, some energy input is required to drive the formation of struvite over time.[24, 26] However, Mg oxidation is a spontaneous process and may not need large overpotentials. Below we provide a literature overview to further aid the reader to recognize the opportunity of (electrochemical) struvite precipitation, as well as to highlight the absence of studies that have focused on the spontaneous oxidation of Mg for struvite precipitation.

Anode:		**Cathode:**
$Mg \leftrightarrow Mg^{+} + e^{-}$		$O_2 + 2H_2O + 4e^{-} \rightarrow 4OH^{-}$ (ORR)
$Mg^{+} + H_2O \rightarrow Mg^{2+} + OH^{-} + 1/2\ H_2 \uparrow$		$H_2O + 2e^{-} \rightarrow 1/2\ H_2 \uparrow + 2OH^{-}$ (HER)

Scheme 1. The main chemical reactions that occur on the anode and cathode surfaces during the electrochemical precipitation of struvite in the pH range of 7.5-9.3.

Hug *et al.* were the first to electrochemically precipitate struvite from source-separated urine by using a Mg alloy plate (type MgAl3Zn1m%) as a sacrificial anode, where the authors applied specific cell voltages to drive the precipitation of struvite through Mg electro-corrosion and reported an energy consumption of ~1.7 $Wh.g^{-1}$ of P.[24] Based upon the same concept, but changing the electrochemical parameters, Zhou *et al.* reported an energy increase from 0.6 to 6.7 $kWh.m^{-3}$ and a specific energy consumption from 2.7 to 29.9 $Wh.g^{-1}$ (as PO_4^{3-}-P) with the increase of applied current from 40 mA to 120 mA, respectively, in the treatment of supernatant resulting from sludge hydrolysis.[36] Liu *et al.* studied the factors influencing the removal of P in wastewater by struvite precipitation using a Mg sacrificial anode and reported an energy consumption of 2.65 $kWh.m^{-3}$, where the electrical energy was supplied by a DC power supply.[37] On the other hand, Ye *et al.* reported an energy consumption between 5.40-11.69 $kWh.kg^{-1}$ of $MgCl_2$ for struvite recovery in seawater by using monovalent selective cation-exchange membranes.[8] Related works include the use of other electrode materials such as Ti, Pt-Ti, Al, Fe, and Al-Mg.[9, 38-41]

As a comparison, we point to an exhaustive, publicly-disseminated report issued in 2014 by the European Commission within the Seventh Framework Programme,[42] where multiple commercial- or pilot-scale chemical precipitation methods for struvite were compared, including a reporting of

energy consumption (as $kWh.kg^{-1}$ P and $kWh.m^{-3}$). These processes and energy consumption metrics include AirPrex® (8 – 16 $kWh.kg^{-1}$ P / 0.5 – 1 $kWh.m^{-3}$), Struvia® (~2 $kWh.kg^{-1}$ P / ≤ 0.3 $kWh.m^{-3}$), Ostara's Pearl® reactor (3.3 $kWh.kg^{-1}$ P / 0.36 – 1.34 $kWh.m^{-3}$), the Gifhorn process (12.9 – 21.6 $kWh.kg^{-1}$ P / 4.5 – 7.6 $kWh.m^{-3}$), and the Stuttgarter Process (3.5 $kWh.kg^{-1}$ P / 8 $kWh.m^{-3}$).[42] While a detailed description of each of these chemical precipitation processes is outside the scope of this paper, we note that the majority of energy consumption data reported in the electrochemical precipitation studies cited above have similar energy requirements at the bench scale, as compared to these pilot-/commercial-scale chemical precipitation data.

One challenge for these P recovery processes is that the traditional biological and chemical P *removal* processes that consider P as a contaminant are likely to consume less energy than P *recovery* processes;[43-48] however, the tremendous downside to these incumbent processes is that all of the P removed is lost to solids waste, which is often sent to landfills. Thus, P *recovery* processes provide an opportunity to re-think wastewater treatment as a resource recovery process, but energy consumption considerations will in part drive technology development and adoption. As such, we pursue our studies of electrochemical struvite precipitation at open circuit potential (OCP) to seek whether the Mg anode driven process can be spontaneous, thus demonstrating this approach as a possibly more energy efficient technology. This strategy would also allow for a profitable fuel resource recovery approach with molecular hydrogen (H_2) produced at both the anode and the cathode during the electrochemical reactions (Scheme 1), thus potentially making the overall process net energy positive.

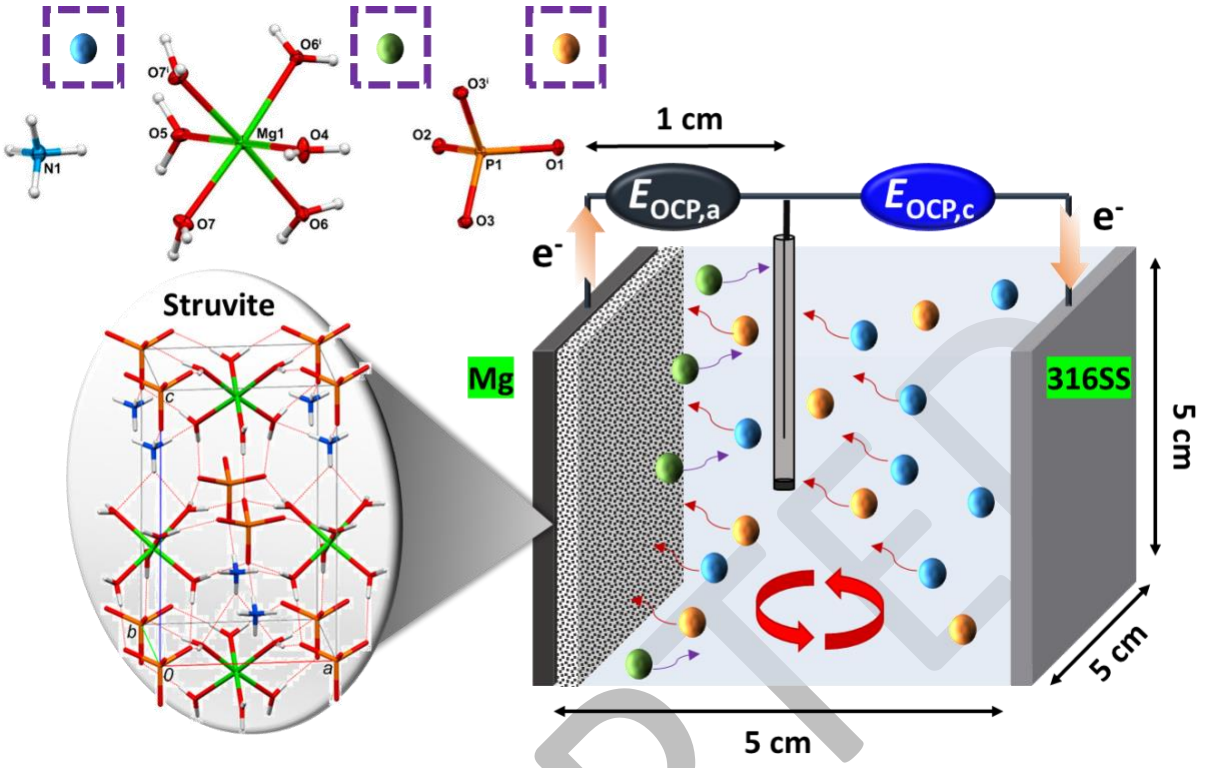

Figure 1. The schematic illustration of the struvite layer formation on the sacrificial magnesium anode during the anodic ($E_{OCP,a}$) and cathodic ($E_{OCP,c}$) open circuit potential measurements. The struvite crystal structure is reprinted with permission from reference [49].

In this study, we hypothesized that spontaneous Mg anode oxidation will drive struvite precipitation without any required energy input, and we investigated how electroless Mg oxidation (i.e., with no applied voltage/current and with the system electrically connected under open circuit potential - OCP) impacts in the chemical structure of struvite, the morphology of precipitates, and the kinetics of the Mg^{2+} dissolution. A bench-scale electrochemical batch reactor was used to produce struvite with no external energy source, and the anodic ($E_{OCP,a}$) and the cathodic ($E_{OCP,c}$) open circuit potentials (OCPs) were monitored over time. Two Mg electrode compositions and a range of reactant concentrations (7.7 – 300 mM) were used to explore the roles of electrode and solution compositions on struvite morphology and Mg^{2+} dissolution kinetics. We have found that under all experimental

conditions tested, struvite was produced at OCP. Our findings are exciting because, under these OCP conditions, the results indicate that struvite production is a thermodynamically favorable process, which could be further be exploited by the growing P recovery and resource recycling industry. Furthermore, we have observed that H_2 was indeed produced during OCP electrochemical struvite precipitation, providing an additional value-add resource. The structure, morphology, and composition of the obtained precipitates were analyzed by Fourier-transform infrared spectrometry (FT-IR), X-ray diffraction (XRD) and scanning electron microscopy (SEM), indicating the production of high quality pure struvite. During the OCP experiments, H_2 production was measured by gas chromatography (GC)-thermal conductivity detector (TCD).

2. MATERIALS AND METHODS

2.1. Materials

All experiments were performed at room temperature (RT) using aqueous solutions containing various amounts (7.7, 77, 150 and 300 mM) of ammonium dihydrogen phosphate ($NH_4H_2PO_4$) from Sigma-Aldrich by using Milli-Q water (18.2MΩ, Millipore, Bedford, MA, USA). The magnesium foil (99.9% pure), the AZ31 magnesium alloy foil (Al 3*wt*%, Zn 1*wt*%, balance Mg) and the stainless-steel (316SS) were all purchased from Goodfellow (USA). The plates were cleaned with different grain size abrasive paper (Norton Abrasives), purchased at a local hardware store. The pH of the bulk test solution was determined before and after the experiments by using a digital pH meter (Orion Star A111, Thermo Scientific). Commercially available struvite distributed and sold as Crystal Green was obtained from Ostara (USA).

2.2. Reactor setup and OCP experiments

The anodic and cathodic open circuit potential (OCP) measurements were conducted in a single-compartment reactor filled with approx. 450 mL of the test solution and continuously stirred at ~220 rpm. The schematic illustration of the experimental setup is shown in Figure 1, where the electrodes are shaped as thin plates with an active surface area of ~40 cm^2 and with a distance between them of 5 cm (note that both sides of the electrodes were used). Either a pure Mg or an AZ31 Mg alloy served as the anode and 316SS as the cathode. The anodic and cathodic OCPs were measured using a VSP-300 multichannel potentiostat/galvanostat (Bio-Logic, USA) and using a double-junction Ag/AgCl (3M NaCl, BASi) reference electrode placed 1 cm away from the anode. The electrical current (I_{Cell}) generated by the overall cell was determined by using a digital multimeter connected to the anode and cathode during the OCP studies.

2.3. Hydrogen gas detection

The detection of H_2 gas formed during the OCP experiments was monitored by using an *H*-cell connected to a 490 Micro GC System (Agilent Technologies, Inc., USA) equipped with a MS5A 10 m Hi-BF column and a micro-machined thermal conductivity detector (TCD). To minimize the interfering effects of the nitrogen and oxygen on the GC chromatograms, the electrolyte was de-aerated by bubbling vigorously with argon (Ar) for 30 min and kept under Ar blanket during the experiments. The samples were analyzed by injecting the sample with a 100 ms injection time from the headspace of the cathode using Ar as the carrier gas for 8 hours, while the injector temperature and the column temperature were both set to 75˚C.

2.4. Struvite crystallization kinetics

For the kinetic studies, determination of the Mg^{2+} and $H_nPO_4^{n-3}$ ionic species in the test solutions was conducted using a dual channel Thermo ICS-6000 ion chromatography system (Thermo Fisher

Scientific, USA) with suppressed conductivity detection and electrolytic eluent generation. Calibration was performed using multi-ion standards IC-2 for anions and IC-CAT6 for cations, both purchased from High Purity Standards, USA. The cations were separated on a CS12A column by using potassium hydroxide (KOH) as eluent, whilst the anions were separated on an AZ19 column by using methane-sulfonic acid (MSA) as eluent. The samples were pre-filtered by using an Acrodisc LC 25mm syringe filter with 0.2 μm PVDF membrane, HPLC certified (Pall Corporation, USA). Anode dissolution rates were determined from gravimetric analysis, in which the mass of the anode plates was determined before and after the 6-hour OCP measurements by using a Mettler Toledo XSE105 dual range analytical balance.

2.5. Surface and material characterization

The elemental composition and morphology of the produced precipitate (struvite) was evaluated by using a scanning electron microscope (SEM, FEI Nova Nanolab 200 Dual-Beam). The crystal structure analysis was performed on a Philips PW1830 double system diffractometer, equipped with a Cu cathode. A Perkin Elmer Frontier FT-IR spectrometer was used to characterize the chemical differences between commercially available struvite and the struvite formed through the experimental electroless process. FT-IR spectrophotometric analysis was carried out using infrared light with 10 wavelength scans from 4,000 cm^{-1} – 650 cm^{-1} at a resolution of 4 cm^{-1}. The distribution of elements of interest within the anode was evaluated by ESI NWR 193 Laser Ablation System (Elemental Scientific Lasers, USA) coupled with a Thermo Scientific iCapQ Quadrupole Mass Spectrometer (LA-ICP-MS) with an image size of 4 cm^2.

3. RESULTS AND DISCUSSION

3.1. Struvite Generation *via* Spontaneous Mg Oxidation

Electrochemical struvite crystallization involves a complex mechanism, where multiple (electro)chemical reactions and processes occur simultaneously over time. In terms of overall struvite production, the corrosion and precipitation reactions that occur cause two major processes: (*i*) corrosion-induced pitting at the anode surface and (*ii*) the formation of struvite, which, if accumulated at the anode surface, can act as an insulating and passivating layer on the sacrificial anode. Based upon previous experiments performed by our group,[27, 34] once the Mg plate is introduced in the ammonium dihydrogen phosphate solution, almost immediately, white struvite particles start to appear on the anode surface. We assume, and further demonstrate through characterization results shown herein, that this precipitate is struvite. Since these experiments were performed within an acidic to neutral pH range, we expected to see struvite, with the formation of hydroxides (e.g., $Mg(OH)_2$) unlikely. The pH is considered an important factor controlling struvite precipitation, where studies have shown the appropriate pH range for precipitates forming high struvite content (>90%) is close to neutral pH.[50] This spontaneous chemical reaction shows that under experimental conditions, a galvanic cell is constructed where an electric potential is produced over time, while struvite is being formed.

Pure Mg and Mg based alloys are reactive metals and thus easily oxidize in humid or wet environments due to their large standard electrode potential ($E^o_{Mg2+/Mg}$ = -2.372 V *vs.* SHE).[51] Furthermore, the E^o values for the acidic hydrogen evolution (HER) and oxygen reduction (ORR) reactions are 0.000 V and 1.229 V *vs.* SHE,[52] respectively. The theoretical (standard) cell potentials (i.e., $E^o_{cell} = E^o_{cathode} - E^o_{anode}$) thus become 3.601 V based on ORR and 2.372 V based on HER, with theoretical Gibb's free energy (ΔG^o) values of -1,389.77 kJ.mol^{-1} and -457.73 kJ.mol^{-1}, respectively.

In the case of alkaline HER and ORR, the E^o values are -0.827 V and +0.401 V vs. SHE,[53] thus the theoretical cell potentials become 2.773 V based on ORR and 1.545 V based on HER, with theoretical ΔG^o values of -1,070.22 kJ.mol^{-1} and -596.28 kJ.mol^{-1}, respectively. These theoretical calculations, while not taking into account system resistance, electrode overpotentials, and reactant concentrations, suggest that the oxidation of the Mg anode should be a spontaneous, thermodynamically-downhill process. However, the operating environment of the anode (e.g., aqueous environment, solution conditions, pit formation, surface passivation) could potentially reduce or prevent Mg corrosion at OCP. To explore the behavior of Mg anode potential under experimental conditions, OCP measurements were obtained (Figure 2) as a function of both reactant concentration and anode type.

Figure 2(a,b) displays the OCP plots as function of time for the pure Mg and the AZ31 alloy plates, respectively, in various ammonium dihydrogen phosphate concentrations. In all cases, an abrupt change in the OCP towards more positive potentials is observed at the beginning of the 6-hour experiment, with a gradual increase in measured anode potential over time after the first hour. Given the known (electro)chemical reactions and processes that occur at the anode surface, we expect the increase in potential to be related to the formation of a passivating film (struvite) on the metallic surface. After the first hour, the slow OCP evolution for the AZ31 Mg alloy suggests the formation of a denser struvite film tightly controls Mg corrosion compared to that of the pure Mg, with a more positive OCP overall. We attribute this difference to the alloy composition and anode surface structure, which could possibly influence struvite precipitation and passivating film morphology through Al and Zn impurities present along the grain boundaries in the anode. The more positive OCP values of the Mg alloy also suggest that the oxidation of Mg from the alloy anode surface is slightly less thermodynamically favorable than from the pure Mg anode surface. In contrast, the measured OCP on the pure Mg anode remains at more negative values but continues to increase towards more positive potentials over the entire 6 hours. This behavior indicates greater Mg corrosion but also a

greater reduction in Mg corrosion over time as struvite precipitation likely continues. Additionally, while the pure Mg anodes (except for the lowest ammonium dihydrogen phosphate concentration) show a simple single increase in anodic potential between 0 and 1 hours (Figure 2(a)), the Mg alloy displays a more complex initial behavior with a small plateau in anodic potential increase at < 1 hour, and a second region where anodic potential increases significantly before leveling off at times > 1 hour (Figure 2(b)).

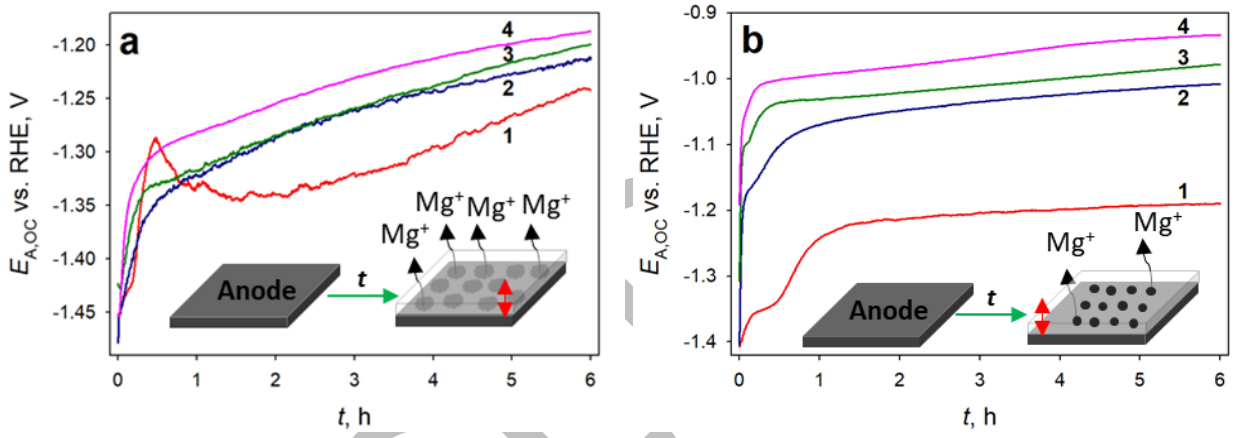

Figure 2. Anodic OCP curves obtained with (a) pure Mg and (b) AZ31 Mg alloy anodes in various concentrations of aqueous ammonium dihydrogen phosphate: (1) 7.7, (2) 77, (3) 150, and (4) 300 mM, respectively.

It should be noted that during the OCP experiments, no struvite formation was observed in the bulk solution or on the cathode, and the struvite formed exclusively on the anode surface. We assume that available sites for heterogeneous precipitation on the Mg plate surface play a major role in struvite crystal formation. In the case of the pure Mg plate, the OCP plots did not attain steady-state potential even after 6 hours, showing a slow and steady increase in potential after 1 hour. This result indicates that struvite precipitation and the dynamic development of the passivating layer on the surface caused increasing thermodynamic losses. It may also indicate that the insulating layer did not form a compact

film on the surface that completely prevents Mg dissolution, and Mg oxidation continued despite the presence of a passivating layer.

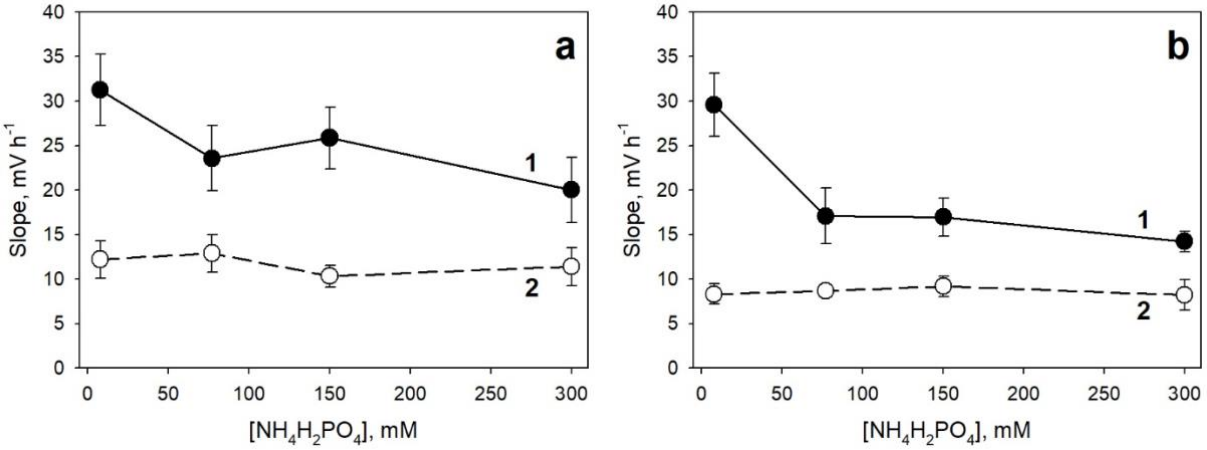

Figure 3. The potential change over time between (a) 1-3- and (b) 3-6-hour time region of the anodic OCP curves obtained with the (1) pure Mg and (2) AZ31 Mg alloy anodes in various concentrations of aqueous ammonium dihydrogen phosphate.

Interestingly, the change in anodic potential over time (slope) determined from the OCP curves between the 1-6-hour time region showed a deviation from linearity, and the analysis of the curves had to be divided into two distinct time regions: 1-3- and 3-6-hour (Figure 3(a,b)). For the pure Mg (filled circles), the results showed a significant decrease in potential over time with the increase of the reactant, which would indicate that the measured OCP is influenced by the characteristics of the insulating layer. Furthermore, for the pure Mg anode, at low salt concentration, the OCP exhibited an interesting behavior, in which the OCP suddenly decreased after ca. 45 min and started to increase again after ca. 2 hours as shown in Figure 2(a) (red line). This behavior may be associated with corrosion-induced pitting, where the formation of the pits increased the active surface area of the anode. Previous studies performed by our group showed that the pits formed were irregular, with an inhomogeneous pattern and large diameter.[34] We propose that once the newly formed pits were filled

with the struvite layer, the OCP started to increase again towards more positive potentials. Additionally, the OCP drop at 45 min may also reflect dynamic changes to the passivating layer properties at the anode surface.

In the case of the AZ31 Mg alloy anode, the OCP plots show different behaviors, whereby two distinct plateaux can be observed as shown in Figure 2(b). At low salt concentrations, the first plateau is observed earlier at ca. 15 min and the second after 60 min. This observation suggests that the formation of the passivating (struvite) layer is occurring in two distinct stages and is likely influenced by the kinetics of struvite crystal formation, film properties, and anodic dissolution. It is possible that in the first stage, a thin layer covers the initial active surface, while in the second stage, more active sites are covered. Thus, the layer becomes thick enough or more compact, which may limit anodic dissolution. The slopes determined from the OCP curves (Figure 3 (a,b)) show practically no change with the increase of the reactant for the alloy anode; thus, the layer formed in all concentrations seem to be uniform and compact in nature after 1 hour. Based upon the shape discrepancy in the obtained OCP curves between the two anode materials, it appears that the corrosion behavior may be affected differently by the formation of struvite and the film properties of the struvite acting as an insulating layer.

3.2. Surface and struvite analysis

After the 6-hour OCP measurements, surface characterization techniques were used to determine the chemistry of the passivating layer and the morphology of the films formed on the sacrificial anode surfaces. For these studies, the precipitated crystals were left on the plates, which were carefully stored and not scraped off as in previous experiments; therefore, the originally formed crystal structure was not altered by any sample processing procedures post-experiment.

The FT-IR spectra recorded (Figure 4(a,b)) show the presence of functional groups previously reported as characteristic of struvite.[51-55] The 3,250-2,900 cm^{-1} band indicated the O-H and N-H stretching vibrations. The H-O-H stretching vibrations are visible at 2,324 cm^{-1}, while the bending region is located at 1,687 cm^{-1}. The N-H bending is represented by a sharp peak at 1,432 cm^{-1}. The symmetric P-O stretching vibration is clearly visible as a strong sharp peak at ~980 cm^{-1} for all samples; however, the asymmetric bending vibration of P-O at 1,168 cm^{-1} is only visible in struvite samples formed on pure-Mg plates. The bands observed at 885-755 cm^{-1} represent the wagging modes of vibration of water molecules. We thus confirm the struvite passivation layer formed on the sacrificial Mg anodes without any energy input during the OCP experiments. These results show that, in our experimental conditions, Mg oxidation is thermodynamically favorable and leads to struvite formation; these results also confirm that precipitates observed (but not chemically identified) in our prior work were likely to have also been struvite.[54] This is an interesting finding as all other previous studies on electrochemical struvite precipitation have used energy input in the form of voltage or current, and no other researchers have attempted to achieve struvite precipitation without the application of voltage or current.

XRD analysis (Figure 4(c,d)) indicated that the white solid layer deposited on the plates during the OCP measurements was composed of high purity struvite. The XRD spectra of the electrochemically obtained struvite on different plates were compared to the commercially available struvite spectrum. The characteristic peaks of the solids were also compared to the struvite standard (PDF card no. 01-077-2303, Figure S1) and found to be close to the struvite pattern (Figure S2(a,b)).

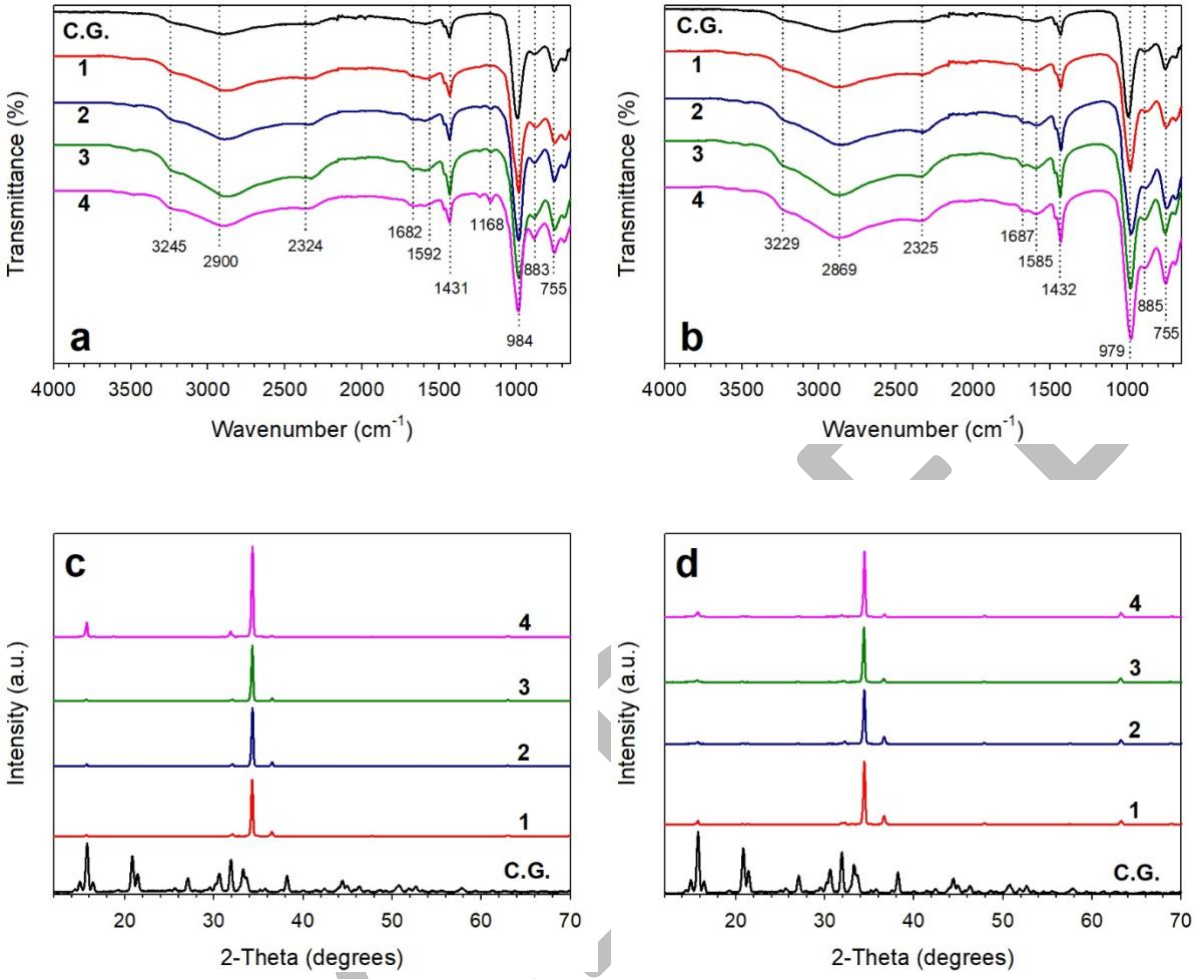

Figure 4. The FT-IR spectra of the struvite formed by OCP on (a) pure Mg, (b) AZ31 Mg alloy; and their respective XRD spectra on (c) pure Mg, (d) AZ31 Mg alloy anodes in various concentrations of the aqueous ammonium dihydrogen phosphate: (1) 7.7, (2) 77, (3) 150, and (4) 300 mM, respectively. Both FT-IR and XRD spectra were compared to the commercially available struvite (Crystal Green, C.G.).

The EDX-determined atomic percentages (At%) of the corresponding elements from the recovered precipitate with both anode types are presented in Figure 5(a,b). In the case of pure Mg, it can be observed that the At% ratio of Mg to P decreased from 3.9±0.5 to 0.9±0.1 (Figure S3) and the At% of Mg to N decreased from 3.5±0.6 to 0.9±0.1 (Figure S4) with the increase of $H_nPO_4^{n-3}/NH_4^+$ in solution. While a theoretical ratio of 1.0 is expected for both, the high ratios obtained at lower reactant

concentrations can be explained by the difference in the thickness of the struvite film formed on the anode surface; for lower reactant concentrations, less struvite likely precipitated on the surface, and the EDX measurement captured some thickness of Mg anode underneath the struvite layer, artificially elevating the Mg At%. In the case of AZ31 Mg alloy, the At% ratio of Mg to P was around 1 regardless of $H_nPO_4^{n-3}/NH_4^+$ (Figure S3). However, the At% of Mg to N decreased from 2.6±0.5 to 0.6±0.1 (Figure S4) with the increase of $H_nPO_4^{n-3}/NH_4^+$ in solution. This result would suggest that there is less ammonium present in the struvite films at lower reactant concentrations and that the struvite film on the alloy anode might be thicker at lower concentrations than its sister film on the pure Mg anode. This result also supports our analysis of the OCP data and slope analysis in Figures 2 and 3, where the pure Mg resulted in a distinct drop in $mV.h^{-1}$ above a concentration of 7.7 mM (Figure 3), suggesting a thin/porous struvite film, while the AZ31 alloy resulted in no change in OCP slope with salt concentration, suggesting thick/dense film formation. The elemental mapping results (see Figure 5(c-j)), revealed a homogeneous distribution of the significant elements (Mg, P and N) in the struvite films.

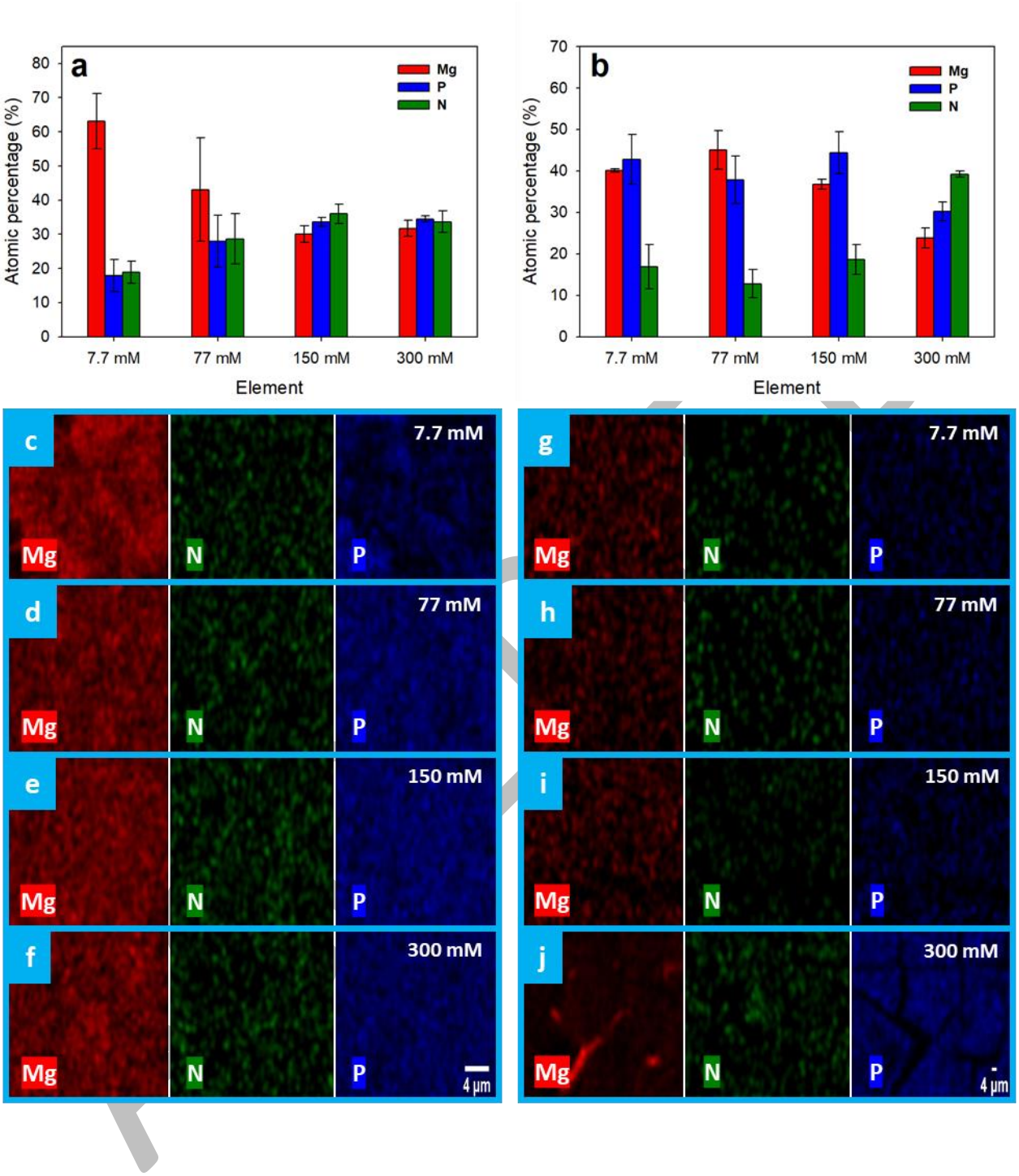

Figure 5. The element atomic percentages (At%) of the struvite layers obtained with the reactor containing the (a) pure Mg; and (b) AZ31 Mg alloy anodes, respectively. The corresponding EDX elemental maps of Mg, N and P for the struvite obtained with the reactor containing (c-f) pure Mg anode; (g-f) AZ31 Mg alloy anode, in various concentrations of the test solution.

For our experimental conditions, struvite was formed in all $H_nPO_4^{n-3}/NH_4^+$ concentrations. Based upon the OCP curves, it was likely that the structure of the struvite film was different for the different anode types and, potentially, for the different reactant concentrations, depending upon the $H_nPO_4^{n-3}/NH_4^+$ concentration or the purity of the Mg anode or both. To determine the morphology of the struvite layer that formed on the Mg anodes, SEM analyses were performed, and the results are shown in Figure 6. For low $H_nPO_4^{n-3}/NH_4^+$ concentrations and the pure Mg anode, the SEM images show a typical crystal morphology[55-58] with a needle-shaped elongated structure (Figure 6(a), red arrows) with a length of ca. 7 µm and a width of ca. 0.8 µm (note that the sharp, smooth edges observed suggest that there are no impurities present in the struvite crystal structure).[13] The increase in $H_nPO_4^{n-3}/NH_4^+$ concentration leads to a significant change in the crystal morphology as shown in Figure 6(b-d, red arrows), from a rod- to an oval-shaped structure with a diameter of ≤ 2 µm. The layer became porous in nature, which likely allowed the solution to reach the anode surface and Mg dissolution to continue to a certain degree even after 6 hours of continuous experiment.

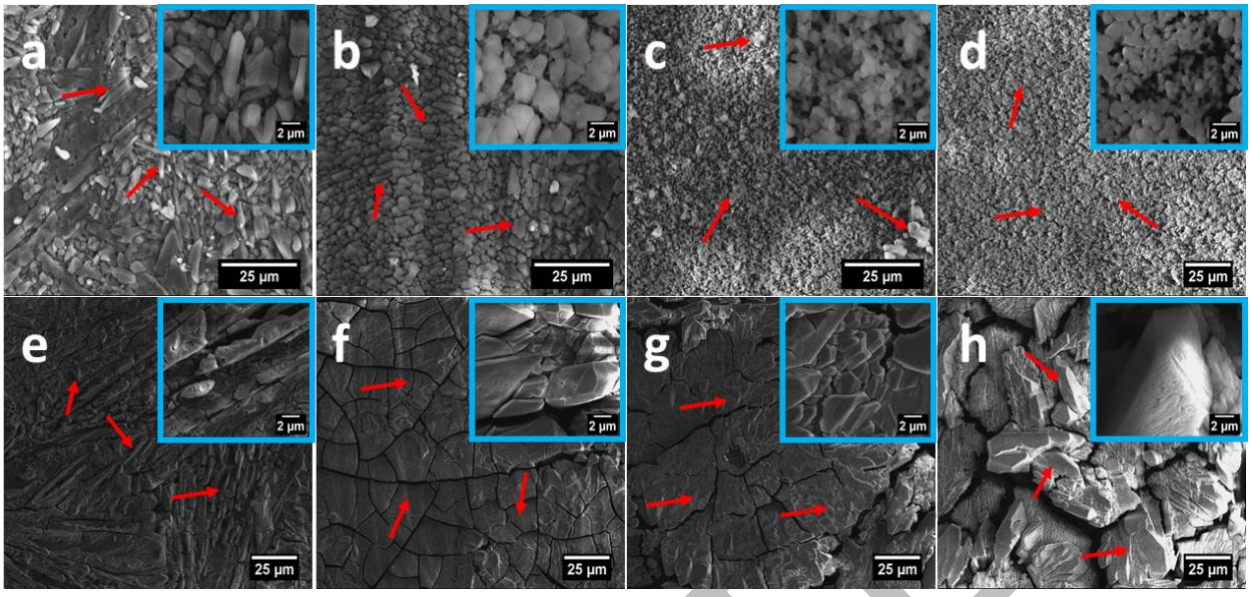

Figure 6. The SEM images obtained of the struvite layer produced on (a-d) pure Mg and (e-h) AZ31 Mg alloy anodes after the 6-hour OCP measurements in 7.7 mM, 77 mM, 150 mM and 300 mM (from left to right) ammonium dihydrogen phosphate aqueous solutions, respectively. Insets: High resolution SEM images showing the change in the struvite structure based on the $H_nPO_4^{n-3}/NH_4^+$ concentrations and the purity of the sacrificial anode.

The SEM images recorded with the struvite films on the AZ31 Mg alloy showed the structure of a uniform and compact layer (Figure 6e-h, red arrows), even at low $H_nPO_4^{n-3}/NH_4^+$ concentrations. The formation of this layer increased the negative effects on the anode performance (i.e. significant electrode fouling and increased operating anode potential), which in turn influenced the overall struvite production in an unfavorable way. This negative effect was successfully demonstrated in our previous studies, where the AZ31 alloy showed only a 5% struvite yield while the pure Mg showed a 38% yield towards struvite production, determined from known amounts of $H_nPO_4^{n-3}/NH_4^+$ in the solution.[34] Moreover, this result could explain the discrepancy found in our earlier studies between the oxidation rates obtained by *Tafel* extrapolation from polarization curves and the Mg dissolution rates obtained from control-potential electrolysis, where the polarization curves indicated a higher

corrosion rate for the AZ31 Mg alloy, while the batch experiments showed higher Mg dissolution rates for the pure Mg anode, respectively.[34]

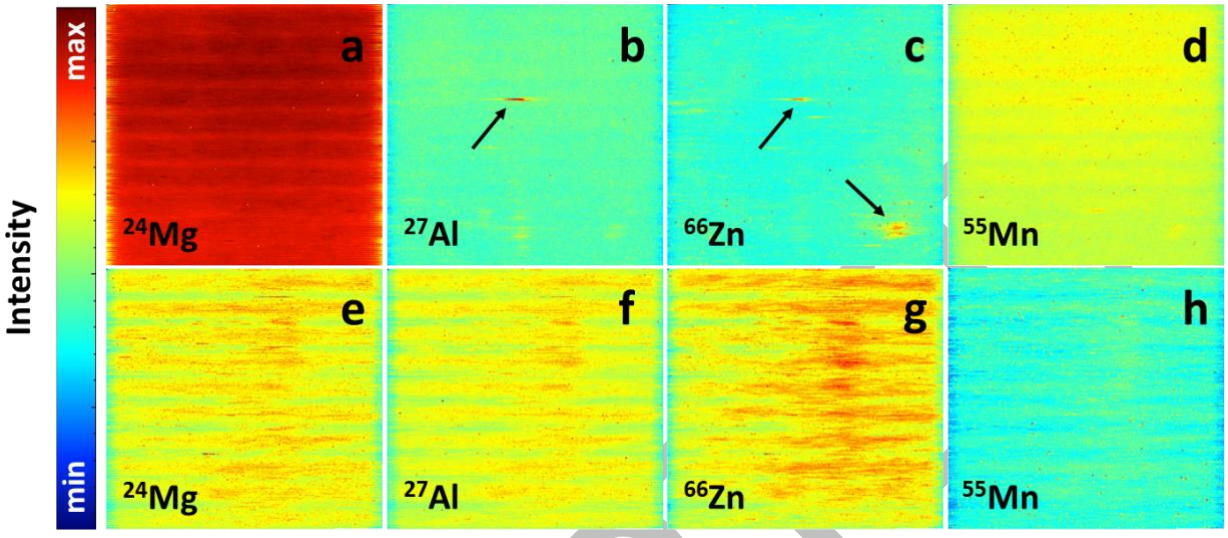

Figure 7. The LA-ICP-MS distribution maps of ^{24}Mg, ^{27}Al, ^{66}Zn, ^{55}Mn recorded with the clean (a-d) pure Mg and (e-h) AZ31 Mg alloy plates. The color scale represents different signal intensities, where blue corresponds to the lowest and red to the highest relative intensity, respectively.

The LA-ICP-MS distribution maps of ^{24}Mg, ^{27}Al, ^{66}Zn, ^{55}Mn of the pure-Mg and AZ31 alloy plates are shown in Figure 7. As expected, the pure Mg plate showed a high abundance for Mg (Figure 7(a)), and low abundance of all other elements, where elements like Al and Zn appeared in small clusters on the surface (Figure 7(b,c), black arrows). On the other hand, the AZ31 Mg alloy showed relatively equal abundances of the elements Mg, Al, and Zn (Figure 7(e-f)), with lower relative abundance of Mg, as compared to the pure Mg anode, and a homogeneous distribution of these elements on the surface. Both anodes presented low intensities with a homogeneous distribution of Mn (Figure 7(d,h)). The findings of this spatial ICP analysis are consistent with our previous study, where a uniform pitting throughout the AZ31 Mg alloy anode was observed, whereas for the pure Mg, a more heterogeneous spatial distribution of pits occurred.[34]

Previous studies have shown that nucleation is the controlling process for struvite formation and is primarily affected by the degree of supersaturation; thus, struvite formation is considered to be a reaction-controlled process.[59-62] In a batch reactor, Mg is often the limiting component during the crystallization process, and hence, the amount of available Mg to form localized high supersaturation regions becomes rather important. For the pure Mg anode, the changes observed in the struvite crystal shape based upon the $H_nPO_4^{n-3}/NH_4^+$ concentrations might be correlated to the struvite crystallization growth kinetics. At high concentrations, the kinetics are expected to be faster, thus smaller crystals with a round shape are formed (Figure 6(c,d)), whereas at low salt concentrations, the kinetics are expected to be considerably slower. In the case of the AZ31 Mg alloy, the crystal growth rates seem likely to be much slower, most likely due to the homogeneous distribution of Zn and Al atoms throughout the alloy structure (Figure 7(f,g)) and the lower relative abundance of Mg at the surface. These impurities considerably limit the ability of the Mg atoms to form a localized supersaturation environment, thus delaying the nucleation process and slowing down the crystal growth rate to a level where a compact insulating layer is formed (Figure 6(e-h)). To investigate the role of kinetics further, an analysis of Mg dissolution and loss of Mg mass from the anodes was followed as a function of time.

3.3. Kinetic analysis of struvite formation

The anodic dissolution of pure Mg and AZ31 Mg alloy plates were studied by gravimetric analysis, where the difference in the mass (Δm) of the plates before and after the 6-hour OCP experiments was recorded in various $H_nPO_4^{n-3}/NH_4^+$ concentrations, see Figure 8(a). Here, the Δm values represent a sum between two changes in the overall mass: (*i*) mass loss of the plate through anodic dissolution and (*ii*) mass of the struvite layer formed on the surface. Both anode types exhibited a linear behavior in their oxidation mass loss with increasing salt concentration (Figure 8(a)), where the pure Mg exhibited higher mass losses for all salt concentrations employed, suggesting a faster anodic

dissolution. The negative Δ*m* values suggest that the mass of the plates is mainly influenced by the anodic dissolution and not by the struvite layer; however, the smaller Δ*m* values recorded with the AZ31 Mg alloy would also suggest that the struvite layer is more compact or thicker compared to the struvite layer formed on the pure Mg, possibly adding additional mass to the plate but also preventing loss of Mg mass through oxidation.

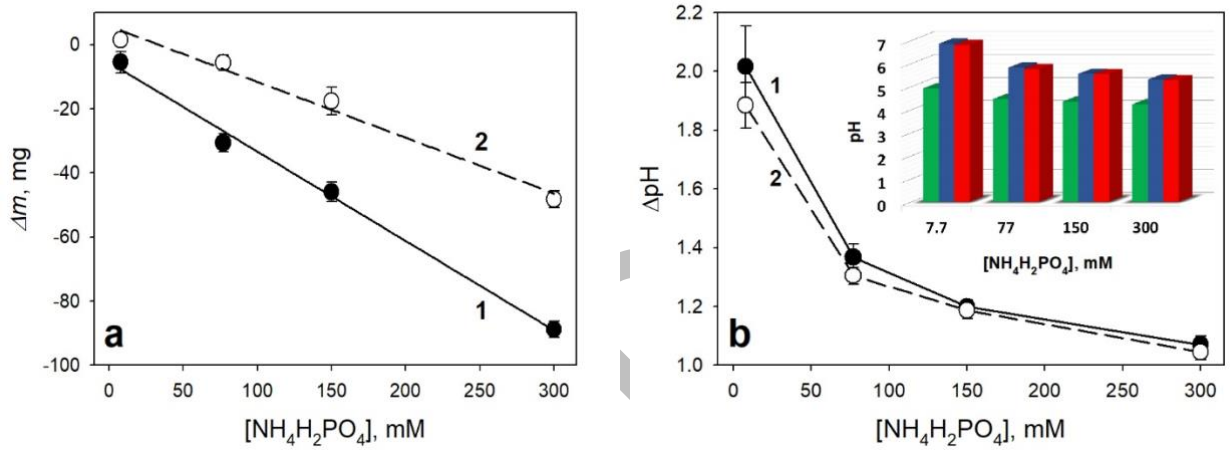

Figure 8. (a) The anode mass losses due to Mg oxidation of the (1) pure Mg and (2) AZ31 Mg alloy plates during the 6-hour OCP measurements. Mass losses are reported as absolute values. (b) pH difference in the bulk solution for various ammonium dihydrogen phosphate concentrations for reactors containing (1) pure Mg and (2) AZ31 Mg alloy as anodes. Inset: the initial pH of the bulk solution (green), the final pH of the bulk solution after 6-hour OCP measurements in case of pure Mg (blue) and AZ31 Mg (red) in various concentrations of the test solution. The reported values represent the average results from four separate experiments (*n*=4) and the error bars the standard deviation.

Struvite nucleation and crystal growth are further controlled and highly influenced by the bulk solution pH; which is an important parameter.[63] The optimal pH for significant struvite precipitation has been reported to be close to neutral pH as a result of ions speciation, where the HPO_4^{2-} and NH_3 concentrations are the highest based upon their speciation profiles.[39, 64-65] On the other hand, Ben

Moussa *et al.*[23] showed that during struvite formation, there is an increase in the local pH at close vicinity of the electrode surface due to the electrochemical reduction of dissolved oxygen or water molecules. Since the bulk solution is continuously stirred throughout the experiments, it is expected that the local pH could influence the bulk pH, which should increase in time. The pH difference in the bulk solution measured before and after the 6-hour OCP measurements in various analyte concentrations are shown in Figure 8(b). As expected, the pH of the bulk solution increased over time, regardless of the anode, see Figure 8(b), inset.

Interestingly, this pH difference gradually decreased with the increase of the test solution concentration: from 2.0 units in 7.7 mM to 1.1 units in 300 mM, see Figure 8(b). Across all concentrations studied, the pH increased from ca. 5 to ca. 7 over 6-hour OCP measurements. This observation can be explained that in the 7.7 mM test solution, the Mg^{2+} concentration far exceeds the $H_nPO_4^{n-3}/NH_4^+$ concentration, with most of the $H_nPO_4^{n-3}/NH_4^+$ ions taking part in the precipitation process and precipitating as struvite. Thus, the amount of OH^- formed during the precipitation at the cathode could greatly influence the bulk pH as the buffering capacity of the phosphate system is lost to solid struvite precipitate. Contrarily, in the 300 mM test solution, where the concentration of $H_nPO_4^{n-3}/NH_4^+$ in the bulk is significantly higher compared to the Mg^{2+} concentration, a lesser relative amount of $H_nPO_4^{n-3}/NH_4^+$ is converted to struvite, and therefore, the OH^- could have a far less effect on the overall pH of the solution.

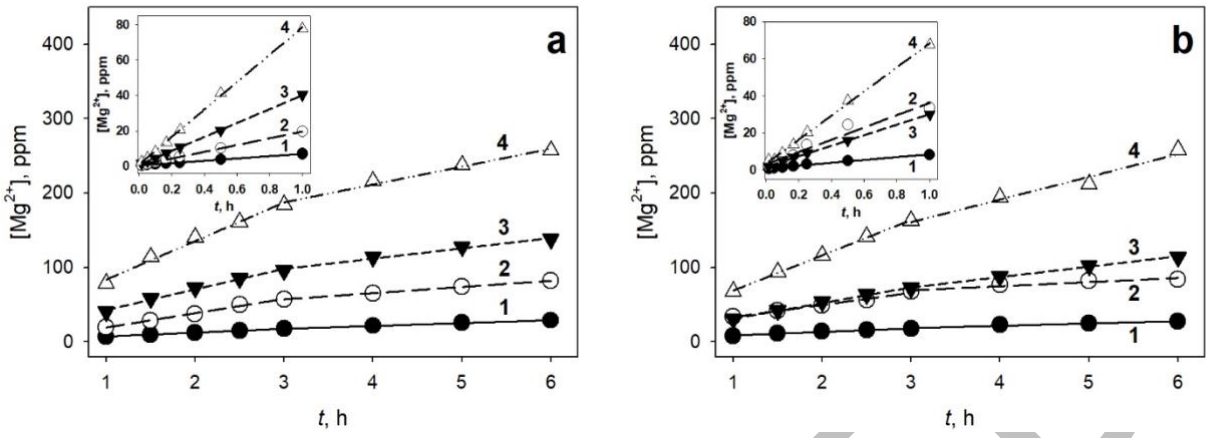

Figure 9. The anodic dissolution of the sacrificial Mg anode (a) pure Mg and (b) AZ31 Mg alloy recorded in: (1) 7.7 mM, (2) 77 mM, (3) 150 mM, and (4) 300 mM ammonium dihydrogen phosphate between 1- and 6-hour time region of the OCP measurements. Insets: The Mg^{2+} dissolution at early time intervals, between 0- and 1-hour time region.

The concentrations of Mg^{2+} product *versus* time during the anodic dissolution of the sacrificial anode are presented in Figure S5, where both anode types displayed a linear behavior primarily applicable between 0- and 3-hour time region. However, after 3 hours, the Mg^{2+} concentration showed a deviation from linear behavior, especially in high concentrations of $H_nPO_4^{n-3}/NH_4^+$, which would suggest that reactions are not zero-order under all conditions and that there is a transition into kinetics of a different order. A more detailed analysis, however, revealed that the Mg dissolution curves actually displayed three different slopes during the 6-hour time period at distinct time regions between 0-1-, 1-3- and 3-6-hour (Figure 9(a,b), with insets), which correlates well with the OCP curves (Figure 2(a,b)). Within these time regions, both anode types showed the formation of Mg^{2+} is independent of the reactant concentration (Mg^0, see Scheme 1), except for the AZ31 Mg alloy at high salt concentration between the 3-6-hour time region, where the Mg^{2+} dissolution followed a first-order

reaction. In this case, the precipitated struvite crystals on the anode surface occupy most of the Mg^0 available surface, and thus the reaction rate may be dependent upon Mg^0 concentration.

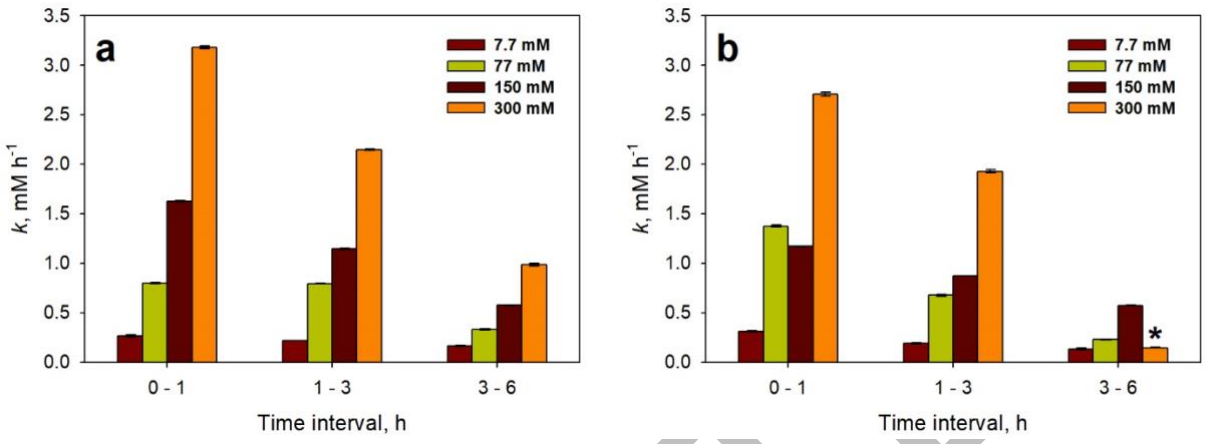

Figure 10. The Mg^{2+} dissolution rate constants for the (a) pure Mg and (b) AZ31 Mg alloy obtained in various concentrations of $H_nPO_4^{n-3}/NH_4^+$ at different time intervals from the OCP curves. *Note: The Mg^{2+} dissolution follows a first-order reaction (h^{-1}).

The overall Mg^{2+} dissolution rate constants (k) obtained from the slopes of the zero-order reactions in various concentrations of $H_nPO_4^{n-3}/NH_4^+$ and distinct time regions with both anodes are presented in Table S1 and are graphically shown in Figure 10(a,b). The k values decrease over time within the same test solution concentration, due to the formation of the struvite layer on the anode surface over time. In the same distinct time interval, k shows an increasing trend with the increase of salt concentration as a result of the higher corrosion rate, see Figure 9(a,b). On the other hand, between 0- and 1-hour time region in low salt concentration (7.7-77 mM), the AZ31 Mg alloy displays higher k values compared to the pure Mg anode, which is the result of the slower struvite crystal formation on the alloy surface.

Table 1. The estimated struvite amount formed on the anode surface, estimated film thickness, the yields, cell voltage, and the Gibb's free energy obtained in various concentrations of $H_nPO_4^{n-3}/NH_4^+$ with different anode types during OCP studies.

Anode	$[NH_4H_2PO_4]$ (mM)	Struvite[a] (mg)	d[b] (µm)	Yield[c] (%)	V_{cell}[d] (V)	ΔG[e] (kJ mol^{-1})
Pure Mg	7.7	4.20±0.10	0.63±0.01	0.50±0.01	1.70±0.01	-327.6±2.3
	77	7.82±1.01	1.17±0.31	0.10±0.01	1.67±0.01	-323.0±1.5
	150	15.95±3.04	2.43±0.42	0.09±0.02	1.62±0.01	-313.3±2.3
	300	26.87±2.52	4.08±0.36	0.08±0.01	1.56±0.01	-301.6±2.4
AZ31 Mg alloy	7.7	10.68±0.48	1.65±0.12	1.27±0.06	1.64±0.02	-316.0±4.7
	77	31.19±2.47	4.67±0.33	0.37±0.03	1.21±0.01	-232.8±1.2
	150	34.71±3.38	5.23±0.42	0.21±0.02	1.17±0.01	-225.7±1.0
	300	67.88±2.67	9.92±0.35	0.20±0.08	1.32±0.01	-254.7±0.9

[a]estimated by gravimetric analysis; [b]struvite film thickness estimated according to Eq. S1; [c]percent yield obtained from the known amount of $H_nPO_4^{n-3}/NH_4^+$ in the test solution; [d]cell potential according to Eq. S2 and [e]Gibb's free energy according to Eq. S3.

The estimated struvite amount formed on the anode surface is presented in Table 1, where the AZ31 Mg alloy under these conditions outperformed the pure Mg in all test solutions. This result is based upon the mass loss measurements (Figure 8) and the Mg^{2+} concentration measurements (Figure 9), where the pure Mg anode exhibited a greater mass loss but Mg^{2+} concentrations measured were similar for the two anode types. The precipitates formed on the alloy showed a ~2.7-fold increase in the film thickness (based on Eq. (S1)) within the same reactant concentration range (7.7 – 300 mM). This calculation assumes a constant density of struvite; and indicates that if the actual film thicknesses

are similar, the struvite film formed on the AZ31 Mg alloy has a higher density than that of the film formed on the pure Mg. This further re-iterates the assumptions made earlier when the OCP curves, SEM images, the anode mass losses were studied, and all suggested the formation of a thicker and/or denser layer on the AZ31 Mg alloy. The calculated cell voltages (V_{cell}, see Eq. S2) show positive values in all reactant concentrations for both anode types, while shifts towards negative cell potentials occur with the increase of the salt, see Table 1. Moreover, the calculated Gibb's free energy values (ΔG, see Eq. S3) are all negative, see Table 1; therefore, for the experimental conditions and setup tested, the production of struvite on the anode is governed by a spontaneous redox reaction. The more positive ΔG values for the AZ31 Mg alloy also suggest that the oxidation of Mg from the alloy surface is slightly less thermodynamically favorable than on the pure Mg anode surface, which is in good agreement with our analysis of OCP behavior and our analysis of struvite film properties.

3.4. Hydrogen production and electricity generation

Next, our study focused on the cathode performance, where the OCP response of the 316SS plate immersed in various $H_nPO_4^{n-3}/NH_4^+$ concentrations was monitored over time (Figure 11(a,b)). The cathode OCP ($E_{C,OC}$) showed a decrease towards more negative potentials over time. However, for the AZ31 Mg alloy anode configuration, the cathode OCP did not exhibit a trend with the increase of the $H_nPO_4^{n-3}/NH_4^+$ concentration (Figure 11(b)). Based upon the chemical reactions showed in Scheme 1, concomitantly with struvite production on the anode surface, di-hydrogen production should occur on the cathode. During OCP experiments, significant bubble formation on the cathode surface was visually confirmed (Figure S6), which could indicate the formation of di-hydrogen.

The di-hydrogen production over the cathode headspace was investigated by GC-TCD in a single salt concentration (120 mM). The chromatograms obtained at the start of the experiments showed the presence of oxygen (O_2) and nitrogen (N_2) in both reactors (Figure 11(c,d)), which are present in the

atmosphere and could not be fully eliminated. On the other hand, towards the end of the experiments the chromatograms clearly exhibited the presence of di-hydrogen (Figure 11(c,d)), while the peaks representing N_2 and O_2 decreased significantly. Both reactors showed a continuous di-hydrogen production over 7 hours (Figure 11(e)) while, the one containing the pure Mg anode produced di-hydrogen after 2 mins (Figure 11(e)), while the AZ31 Mg alloy anode started to produce di-hydrogen after 1.5 hours (Figure 11(e)). The fluctuation observed in the di-hydrogen production over time within both reactors is beyond the scope of this paper and will be studied in future work. The difference in time to the onset of H_2 production for pure Mg vs. AZ31 Mg alloy anodes suggests significant differences in the operational thermodynamics of the overall electrochemical cell, where the larger cell voltages and calculated Gibb's free energy values for the pure Mg indicate a greater energetic driving force for both Mg corrosion and cathodic reduction reactions such as H_2 production (i.e., the hydrogen evolution reaction, HER).

The generation of electricity with the proposed reactors was also studied and the results are shown in Figure 11(f). As expected, both reactors (i.e., both Mg anode compositions) were able to produce electricity, which decreased over time following the same trend discussed above, due to the struvite layer formation on the anode. The reactor containing the pure Mg anode started at -39.8 mA and decreased over time reaching -12.4 mA, while the current for the AZ31 Mg alloy reactor decreased from -30.4 mA to -14.6 mA, see Figure 11(f). The lower current produced by the AZ31 Mg alloy further supports the differences in the operational thermodynamics between the two reactors. Furthermore, the more modest current decrease observed for the AZ31 Mg alloy can be correlated to the more compact struvite layer formation.

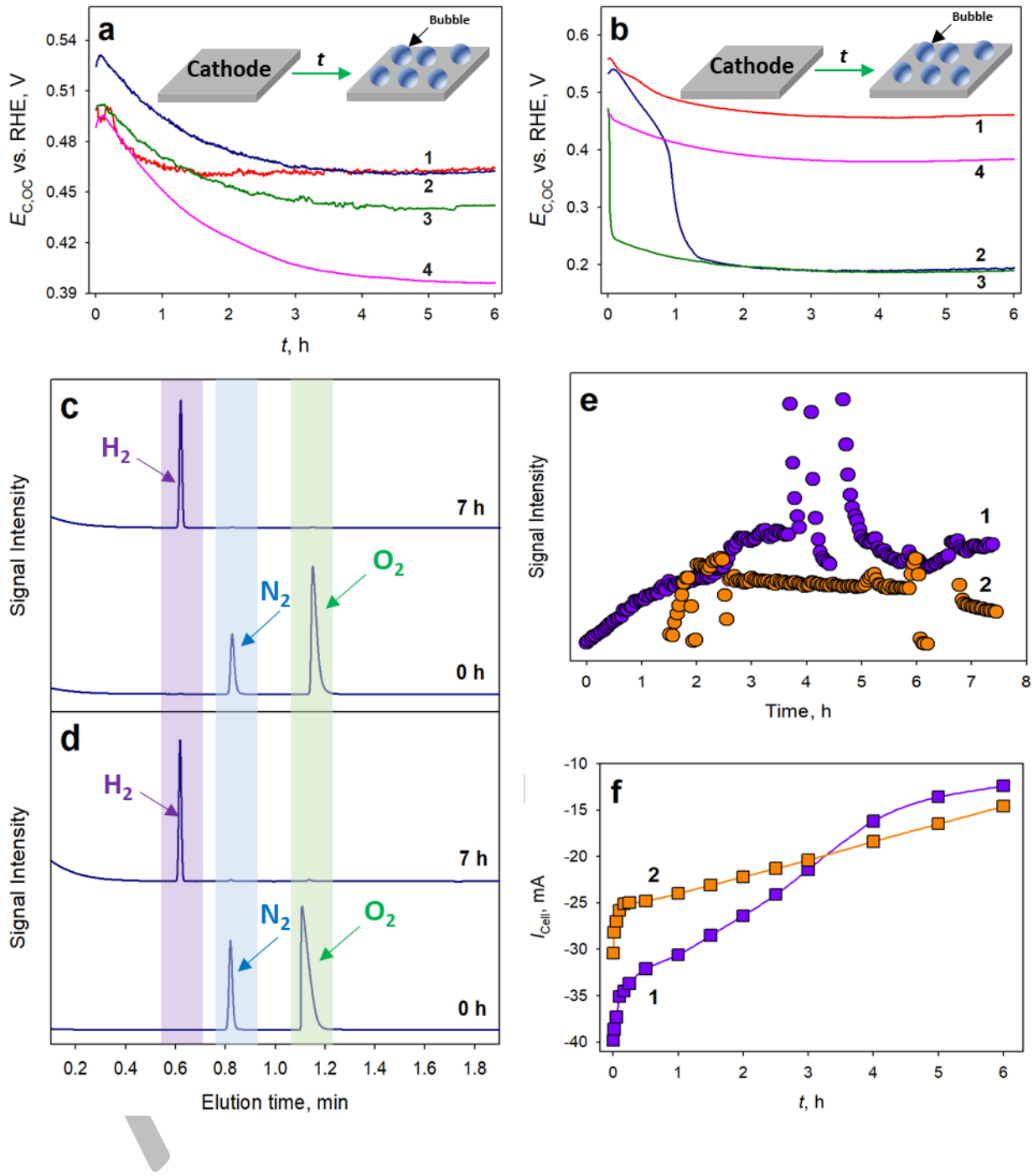

Figure 11. Cathodic OCP curves obtained with 316SS plates for reactors where (a) pure Mg and (b) AZ31 Mg alloy were the anodes in: (1) 7.7, (2) 77, (3) 150, and (4) 300 mM $H_nPO_4^{n-3}/NH_4^+$, respectively. The chromatograms recorded using a GC-TCD over the 316SS cathode headspace in the *H*-cell at different time intervals with reactor where (c) pure Mg and (d) AZ31 Mg alloy were the anodes, respectively. (e)

Hydrogen production evolution over the 6-hour time period measured at the 316SS cathode headspace, and (f) measured overall cell current (i.e., electricity produced) where (1) pure Mg or (2) AZ31 Mg alloy were the anodes, respectively.

3.5. Nutrient removal from a natural agricultural wastewater

In the next step, we looked at the practical implementation of the reactor in a ”real world scenario”, where we investigated the electroless nutrient removal from a natural poultry wastewater (PWW) sample. To avoid a possible co-precipitate alongside the struvite due to the impurities present in the Mg alloy structure, we decided to use only the pure Mg as the anode. Furthermore, the raw wastewater sample was pretreated by using a crossflow membrane filtration system (NB: see detailed description in the *ESI*) to remove the suspended solids. The compositions of the raw-, pretreated-, and post-OCP study PWW are presented in Table S2. The anodic/cathodic OCP plots as function of time in the PWW are displayed in Figure 12(a) and show similar behavior as in the synthetic wastewater (Figure 2(a)). During the 6-hour OCP measurement, an increase in the bulk solution pH from 9.0 to 9.8 was observed.

Under these conditions, the reactor was able to remove ~73% of the $H_nPO_4^{n-3}$ present in the PWW, while concomitantly di-hydrogen was formed (Figure 12(b)). Interestingly, most of the $H_nPO_4^{n-3}$ was removed in the 0-3-hour interval, while most of the di-hydrogen produced was in the 3-6-hour interval. This impressive $H_nPO_4^{n-3}$ removal can be explained based upon the equilibrium between the three forms of the phosphate ion, where HPO_4^{2-} was the dominant species for the PWW pH range of 9.1 – 9.8, while in alkaline solutions the PO_4^{3-} (HPO_4^{2-}/PO_4^{3-} pK_a is ~12.67) form dominates. Further, the pH remained below the point where other species (e.g., $Mg(OH)_2$) would dominate precipitation. The XRD spectrum of the obtained precipitate in this complex matrix was compared to the electrochemically obtained struvite in the synthetic wastewater and was found to have similar

diffraction peaks, Figure 12(c). The SEM images obtained in Figure 12(d) show similarities to a struvite crystal morphology.

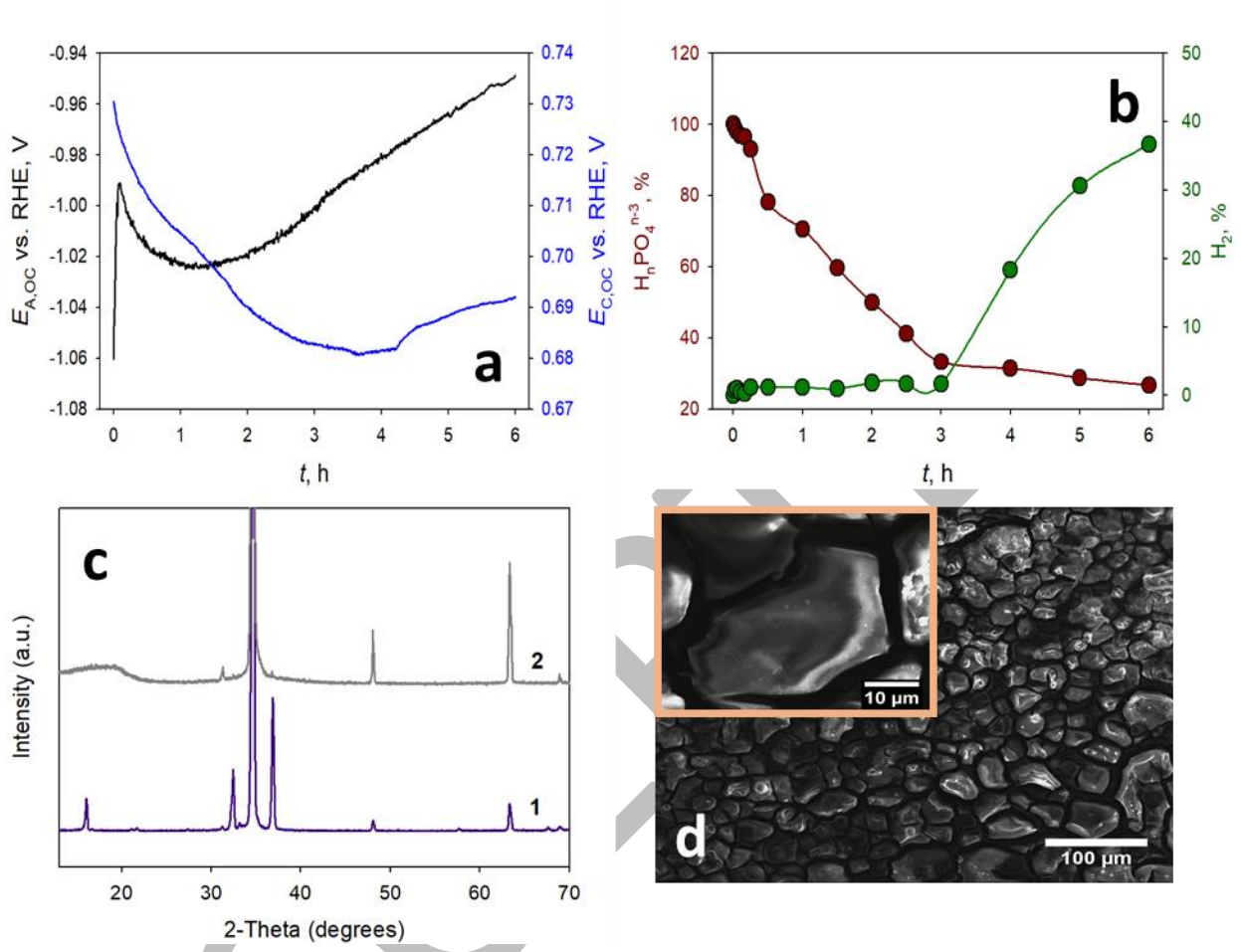

Figure 12. (a) Anodic/cathodic OCP curves obtained for the reactor with pure Mg and 316SS plates. (b) Phosphate removal and di-hydrogen production over time in a poultry wastewater sample. (c) XRD spectra of the struvite formed in (1) synthetic and (2) poultry wastewaters samples, respectively. (d) SEM image obtained of the struvite layer produced on the anode in a poultry wastewater sample. Inset: High resolution SEM image.

4. Conclusions

The present study provides insight towards electroless synthesis of both magnesium ammonium phosphate hexahydrate, also known as struvite, and di-hydrogen. We demonstrate struvite and H_2 production from either pure Mg or Mg alloy as anodes and 316SS as cathode respectively, where the precipitate was obtained with zero energy input. Both pure Mg and AZ31 Mg alloy anodes acted as reliable sources for Mg^{2+} ions. The impurities present in the grain structure of the alloy negatively influenced local supersaturation, which produced significant changes to the struvite morphology and crystal structure, thus forming a uniform and compact layer. Contrarily, pure Mg anode produced a porous struvite film, especially in highly concentrated $H_nPO_4^{n-3}/NH_4^+$. Interestingly, while the oxidation rate of Mg from the pure Mg anode was higher, the estimated mass of struvite formed was less than that of the Mg alloy anode. Various surface characterization techniques indicated that the struvite obtained on the anode surface was of high quality. Kinetic analyses showed that Mg^{2+} dissolution followed a zero-order reaction for both anode types, except for the alloy at higher salt concentrations between the 3-6-hour time region, where the Mg^{2+} dissolution followed a first-order reaction. The Mg^{2+} dissolution rate constants showed a dependence on $H_nPO_4^{n-3}/NH_4^+$ concentration and precipitate layer formation. Concomitantly with struvite formation on the anode, di-hydrogen was produced at the cathode over time. Furthermore, we fully demonstrated the performance of the reactor under realistic conditions, in which 73% of the $H_nPO_4^{n-3}$ present in a poultry wastewater sample was removed as mainly struvite. Our early findings could pave the way to further explore possibilities for sustainable phosphorous recovery from wastewaters by using green technologies that would provide energy and environmental benefits.

Acknowledgements

LKN and LFG acknowledge the National Science Foundation (NSF) for the financial support of this work through the INFEWS/T3 Award# 1739473 and the University of Arkansas Institute for Nanoscience and Nanotechnology characterization facility for support in surface and material characterization. We thank Dr. Barry Shaulis and Mr. Erik Pollock from the Trace Element and Radiogenic Isotope Lab for their help with the LA-ICP-MS-Mapping and IC analaysis. We are also grateful to Dr. Jamie A. Hestekin from University of Arkansas for allowing us to perform the FTIR analysis. The authors thank John Askegaard for supplying natural wastewater samples of poultry condensate for testing.

References

1. Rasmussen, L. V.; Coolsaet, B.; Martin, A.; Mertz, O.; Pascual, U.; Corbera, E.; Dawson, N.; Fisher, J. A.; Franks, P.; Ryan, C. M., Social-ecological outcomes of agricultural intensification. *Nat. Sustain.* **2018,** *1* (6), 275.

2. Tilman, D.; Balzer, C.; Hill, J.; Befort, B. L., Global food demand and the sustainable intensification of agriculture. *Proc. Natl. Acad. Sci. U.S.A* **2011,** *108* (50), 20260-20264.

3. Rudel, T. K.; Schneider, L.; Uriarte, M.; Turner, B. L.; DeFries, R.; Lawrence, D.; Geoghegan, J.; Hecht, S.; Ickowitz, A.; Lambin, E. F., Agricultural intensification and changes in cultivated areas, 1970–2005. *Proc. Natl. Acad. Sci. U.S.A* **2009,** *106* (49), 20675-20680.

4. Castine, S. A.; McKinnon, A. D.; Paul, N. A.; Trott, L. A.; de Nys, R., Wastewater treatment for land-based aquaculture: improvements and value-adding alternatives in model systems from Australia. *Aquacult. Environ. Interac.* **2013,** *4* (3), 285-300.

5. Li, B.; Boiarkina, I.; Yu, W.; Huang, H. M.; Munir, T.; Wang, G. Q.; Young, B. R., Phosphorous recovery through struvite crystallization: challenges for future design. *Sci. Total. Environ.* **2019,** *648*, 1244-1256.

6. Türker, M.; Çelen, I., Removal of ammonia as struvite from anaerobic digester effluents and recycling of magnesium and phosphate. *Bioresour. Technol.* **2007,** *98* (8), 1529-1534.

7. Godfray, H. C. J.; Beddington, J. R.; Crute, I. R.; Haddad, L.; Lawrence, D.; Muir, J. F.; Pretty, J.; Robinson, S.; Thomas, S. M.; Toulmin, C., Food security: the challenge of feeding 9 billion people. *Science* **2010,** *327* (5967), 812-818.

8. Ye, Z.-L.; Ghyselbrecht, K.; Monballiu, A.; Rottiers, T.; Sansen, B.; Pinoy, L.; Meesschaert, B., Fractionating magnesium ion from seawater for struvite recovery using electrodialysis with monovalent selective membranes. *Chemosphere* **2018,** *210*, 867-876.

9. Lei, Y.; Du, M.; Kuntke, P.; Saakes, M.; van der Weijden, R.; Buisman, C. J. N., Energy efficient phosphorus recovery by microbial electrolysis cell induced calcium phosphate precipitation. *ACS Sustain. Chem. Eng.* **2019,** *7* (9), 8860-8867.

10. Zhang, Z.; She, L.; Zhang, J.; Wang, Z.; Xiang, P.; Xia, S., Electrochemical acidolysis of magnesite to induce struvite crystallization for recovering phosphorus from aqueous solution. *Chemosphere* **2019,** *226*, 307-315.

11. Massey, M. S.; Davis, J. G.; Ippolito, J. A.; Sheffield, R. E., Effectiveness of recovered magnesium phosphates as fertilizers in neutral and slightly alkaline soils. *Agronomy J.* **2009,** *101* (2), 323-329.

12. Shu, L.; Schneider, P.; Jegatheesan, V.; Johnson, J., An economic evaluation of phosphorus recovery as struvite from digester supernatant. *Biores. Technol.* **2006,** *97* (17), 2211-2216.

13. Le Corre, K. S.; Valsami-Jones, E.; Hobbs, P.; Parsons, S. A., Impact of calcium on struvite crystal size, shape and purity. *J. Cryst. Growth* **2005,** *283* (3-4), 514-522.

14. Huchzermeier, M. P.; Tao, W., Overcoming challenges to struvite recovery from anaerobically digested dairy manure. *Water Environ. Res.* **2012,** *84* (1), 34-41.

15. Kim, J. H.; min An, B.; Lim, D. H.; Park, J. Y., Electricity production and phosphorous recovery as struvite from synthetic wastewater using magnesium-air fuel cell electrocoagulation. *Water Res.* **2018,** *132*, 200-210.

16. Zeng, F.; Zhao, Q.; Jin, W.; Liu, Y.; Wang, K.; Lee, D.-J., Struvite precipitation from anaerobic sludge supernatant and mixed fresh/stale human urine. *Chem. Eng. J.* **2018,** *344*, 254-261.

17. Abel-Denee, M.; Abbott, T.; Eskicioglu, C., Using mass struvite precipitation to remove recalcitrant nutrients and micropollutants from anaerobic digestion dewatering centrate. *Water Res.* **2018,** *132*, 292-300.

18. Wang, F.; Fu, R.; Lv, H.; Zhu, G.; Lu, B.; Zhou, Z.; Wu, X.; Chen, H., Phosphate recovery from swine wastewater by a struvite precipitation electrolyzer. *Sci. Rep.* **2019,** *9* (1), 8893.

19. Shu, J.; Wu, H.; Chen, M.; Peng, H.; Li, B.; Liu, R.; Liu, Z.; Wang, B.; Huang, T.; Hu, Z., Fractional removal of manganese and ammonia nitrogen from electrolytic metal manganese residue leachate using carbonate and struvite precipitation. *Water Res.* **2019,** *153*, 229-238.

20. Lin, X.; Han, Z.; Yu, H.; Ye, Z.; Zhu, S.; Zhu, J., Struvite precipitation from biogas digestion slurry using a two-chamber electrolysis cell with a magnesium anode. *J. Clean. Prod.* **2018,** *174*, 1598-1607.

21. Merino-Jimenez, I.; Celorrio, V.; Fermin, D. J.; Greenman, J.; Ieropoulos, I., Enhanced MFC power production and struvite recovery by the addition of sea salts to urine. *Water Research* **2017,** *109*, 46-53.

22. You, J.; Greenman, J.; Melhuish, C.; Ieropoulos, I., Electricity generation and struvite recovery from human urine using microbial fuel cells. *Journal of Chemical Technology & Biotechnology* **2016,** *91* (3), 647-654.

23. Ben Moussa, S.; Maurin, G.; Gabrielli, C.; Amor, M. B., Electrochemical precipitation of struvite. *Electrochem. Solid State Lett.* **2006,** *9* (6), C97-C101.

24. Hug, A.; Udert, K. M., Struvite precipitation from urine with electrochemical magnesium dosage. *Water Res.* **2013,** *47* (1), 289-299.

25. Ren, S.; Li, M.; Sun, J.; Bian, Y.; Zuo, K.; Zhang, X.; Liang, P.; Huang, X., A novel electrochemical reactor for nitrogen and phosphorus recovery from domestic wastewater. *Front. Env. Sci. Eng.* **2017,** *11* (4), 17.

26. Kruk, D. J.; Elektorowicz, M.; Oleszkiewicz, J. A., Struvite precipitation and phosphorus removal using magnesium sacrificial anode. *Chemosphere* **2014,** *101*, 28-33.

27. Kékedy-Nagy, L.; Teymouri, A.; Herring, A. M.; Greenlee, L. F., Electrochemical removal and recovery of phosphorus as struvite in an acidic environment using pure magnesium vs. the AZ31 magnesium alloy as the anode. *Chem. Eng. J.* **2019**, 122480.

28. Inan, H.; Alaydın, E., Phosphate and nitrogen removal by iron produced in electrocoagulation reactor. *Desal. Water Treat.* **2014,** *52* (7-9), 1396-1403.

29. Huang, H.; Zhang, D.; Zhao, Z.; Zhang, P.; Gao, F., Comparison investigation on phosphate recovery from sludge anaerobic supernatant using the electrocoagulation process and chemical precipitation. *J. Clean. Prod.* **2017,** *141*, 429-438.

30. Zheng, X.-y.; Kong, H.-N.; Wu, D.-y.; Wang, C.; Li, Y.; Ye, H.-r., Phosphate removal from source separated urine by electrocoagulation using iron plate electrodes. *Water Sci. Technol.* **2009,** *60* (11), 2929-2938.

31. Mores, R.; Treichel, H.; Zakrzevski, C. A.; Kunz, A.; Steffens, J.; Dallago, R. M., Remove of phosphorous and turbidity of swine wastewater using electrocoagulation under continuous flow. *Sep. Purif. Technol.* **2016,** *171*, 112-117.

32. Oumar, D.; Patrick, D.; Gerardo, B.; Rino, D.; Ihsen, B. S., Coupling biofiltration process and electrocoagulation using magnesium-based anode for the treatment of landfill leachate. *J. Enviro. Manage.* **2016,** *181*, 477-483.

33. Ledezma, P.; Kuntke, P.; Buisman, C. J. N.; Keller, J.; Freguia, S., Source-separated urine opens golden opportunities for microbial electrochemical technologies. *Trends Biotechnol.* **2015,** *33* (4), 214-220.

34. Kékedy-Nagy, L.; Moore, J. P.; Abolhassani, M.; Attarzadeh, F.; Hestekin, J. A.; Greenlee, L. F., The passivating layer influence on Mg-based anode corrosion and implications for electrochemical struvite precipitation. *J. Electrochem. Soc.* **2019,** *166* (12), E358-E364.

35. Song, G. L.; Atrens, A., Corrosion mechanisms of magnesium alloys. *Adv. Eng. Mater.* **1999,** *1*, 11-33.

36. Zhou, X.; Chen, Y., An integrated process for struvite electrochemical precipitation and ammonia oxidation of sludge alkaline hydrolysis supernatant. *Environ. Sci. Pollut. Res.* **2019,** *26* (3), 2435-2444.

37. Liu, W.; Li, J.; He, X.; Wang, Z.; Chun, Z., Factors influencing the removal of phosphorus and the purity of recycling struvite in wastewater by the electrochemical sacrificial magnesium anode method. *Sci. Adv. Mater.* **2019,** *11* (1), 128-134.

38. Yuan, P.; Kim, Y., Increasing phosphorus recovery from dewatering centrate in microbial electrolysis cells. *Biotechnol. Biofuels* **2017,** *10* (1), 70.

39. Kiani, D.; Sheng, Y.; Lu, B.; Barauskas, D.; Honer, K.; Jiang, Z.; Baltrusaitis, J., Transient struvite formation during stoichiometric (1:1) NH_4^+ and PO_4^{3-} adsorption/reaction on magnesium oxide (MgO) particles. *ACS Sustain. Chem. Eng.* **2018,** *7* (1), 1545-1556.

40. Nasr, M.; Ateia, M.; Hassan, K., Artificial intelligence for greywater treatment using electrocoagulation process. *Sep. Sci. Technol.* **2016,** *51* (1), 96-105.

41. Dura, A.; Breslin, C. B., Electrocoagulation using aluminium anodes activated with Mg, In and Zn alloying elements. *J. Hazard. Mater.* **2019,** *366*, 39-45.

42. Ewert, W.; Hermanussen, O.; Kabbe, C.; Mele, C.; Niewersch, C.; Paillard, H.; Stossel, E.; Wagenbach, A.; Stemann, J. *Sustainable sewage sludge management fostering phosphorus recovery and energy efficiency*; http://www.p-rex.eu/fileadmin/P-REX-Reserach/Downloads/P-REX_D_5_online.pdf, 2014.

43. Bashar, R.; Gungor, K.; Karthikeyan, K. G.; Barak, P., Cost effectiveness of phosphorus removal processes in municipal wastewater treatment. *Chemosphere* **2018,** *197*, 280-290.

44. Singh, P.; Carliell-Marquet, C.; Kansal, A., Energy pattern analysis of a wastewater treatment plant. *Appl. Water Sci.* **2012,** *2* (3), 221-226.

45. Tunçal, T.; İşgenç, F.; Pala, A., Importance of EBPR efficiency on energy demand of full-scale wastewater treatment plants. *Desal. Water Treat.* **2010,** *22* (1-3), 292-298.

46. Bertanza, G.; Menoni, L.; Capoferri, G. U.; Pedrazzani, R., Promoting biological phosphorus removal in a full scale pre-denitrification wastewater treatment plant. *J. Environ. Manage.* **2020,** *254*, 109803.

47. Levlin, E.; Hultman, B. In *Phosphorus recovery from phosphate rich side-streams in wastewater treatment plants*, Polish Swedish seminar, Gdansk March, 2003; pp 23-25.

48. Ødegaard, H., An evaluation of cost efficiency and sustainability of different wastewater treatment processes. *Vatten* **1995,** *51*, 291-299.

49. Prywer, J.; Sieroń, L.; Czylkowska, A., Struvite grown in gel, its crystal structure at 90 K and thermoanalytical study. *Crystals* **2019,** *9* (2), 89.

50. Hao, X.; Wang, C.; van Loosdrecht, M. C. M.; Hu, Y., Looking Beyond Struvite for P-Recovery. *Environ. Sci. Technol.* **2013,** *47* (10), 4965-4966.

51. Coates, G. E., 124. The standard electrode potential of magnesium. *Journal of the Chemical Society (Resumed)* **1945,** (0), 478-479.

52. Suen, N.-T.; Hung, S.-F.; Quan, Q.; Zhang, N.; Xu, Y.-J.; Chen, H. M., Electrocatalysis for the oxygen evolution reaction: recent development and future perspectives. *Chemical Society Reviews* **2017,** *46* (2), 337-365.

53. Ge, X.; Sumboja, A.; Wuu, D.; An, T.; Li, B.; Goh, F. W. T.; Hor, T. S. A.; Zong, Y.; Liu, Z., Oxygen Reduction in Alkaline Media: From Mechanisms to Recent Advances of Catalysts. *ACS Catalysis* **2015,** *5* (8), 4643-4667.

54. Foroughi, F.; Kékedy-Nagy, L.; Islam, M. H.; Lamb, J. J.; Greenlee, L. F.; Pollet, B. G., The use of ultrasound for the electrochemical synthesis of magnesium ammonium phosphate hexahydrate (struvite). *ECS Trans.* **2019,** *92* (10), 47-55.

55. Li, H.; Yu, S.-H.; Yao, Q.-Z.; Zhou, G.-T.; Fu, S.-Q., Chemical control of struvite scale by a green inhibitor polyaspartic acid. *RSC Adv.* **2015,** *5* (111), 91601-91608.

56. Belarbi, Z.; Trembly, J. P., Electrochemical processing to capture phosphorus from simulated concentrated animal feeding operations waste. *J. Electrochem. Soc.* **2018,** *165* (13), E685-E693.

57. Graeser, S.; Postl, W.; Bojar, H.-P.; Berlepsch, P.; Armbruster, T.; Raber, T.; Ettinger, K.; Walter, F., Struvite-(K), $KMgPO_4 \cdot 6H_2O$, the potassium equivalent of struvite–a new mineral. *Eur. J. Mineral* **2008,** *20* (4), 629-633.

58. Whitaker, A.; Jeffery, J. W., The crystal structure of struvite, $MgNH_4PO_4.\ 6H_2O$. *Acta Crystallogr. B* **1970,** *26* (10), 1429-1440.

59. Doyle, J. D.; Oldring, K.; Churchley, J.; Parsons, S. A., Struvite formation and the fouling propensity of different materials. *Water Res.* **2002,** *36* (16), 3971-3978.

60. Mehta, C. M.; Batstone, D. J., Nucleation and growth kinetics of struvite crystallization. *Water Res.* **2013,** *47* (8), 2890-2900.

61. Agrawal, S.; Guest, J. S.; Cusick, R. D., Elucidating the impacts of initial supersaturation and seed crystal loading on struvite precipitation kinetics, fines production, and crystal growth. *Water Res.* **2018,** *132*, 252-259.

62. Crutchik, D.; Garrido, J. M., Kinetics of the reversible reaction of struvite crystallisation. *Chemosphere* **2016,** *154*, 567-572.

63. Ohlinger, K. N.; Young, T. M.; Schroeder, E. D., Predicting struvite formation in digestion. *Water Res.* **1998,** *32* (12), 3607-3614.

64. Tansel, B.; Lunn, G.; Monje, O., Struvite formation and decomposition characteristics for ammonia and phosphorus recovery: A review of magnesium-ammonia-phosphate interactions. *Chemosphere* **2018,** *194*, 504-514.

65. Jaffer, Y.; Clark, T. A.; Pearce, P.; Parsons, S. A., Potential phosphorus recovery by struvite formation. *Water Res.* **2002,** *36* (7), 1834-1842.

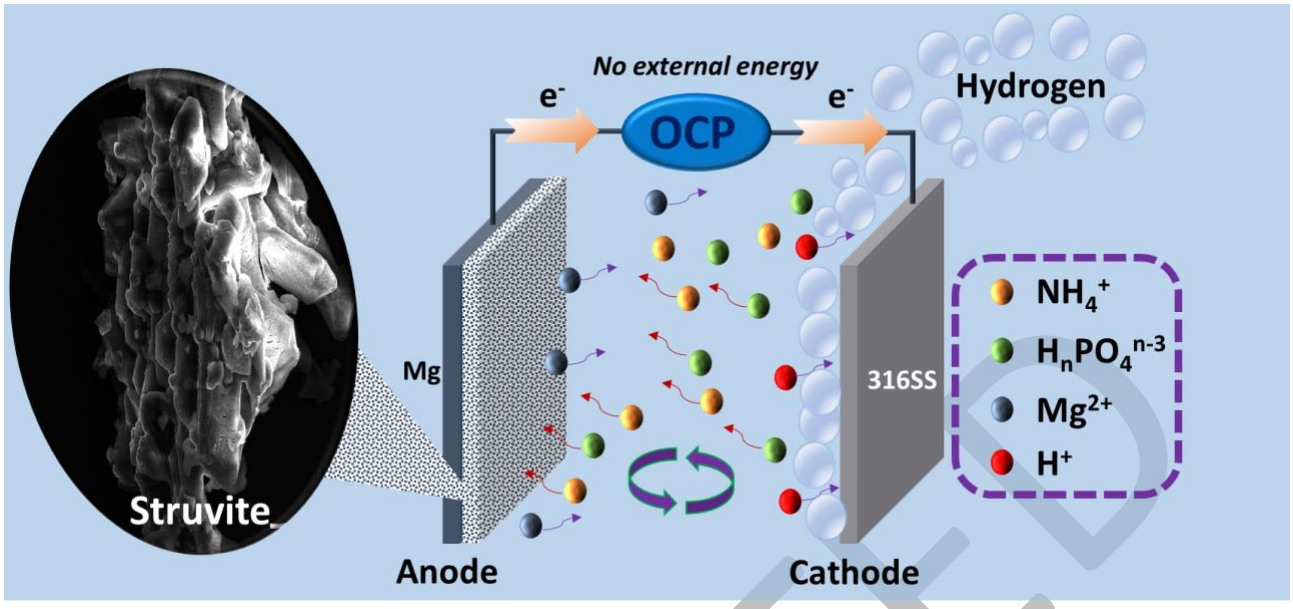
No external energy
e-
e-
OCP
Hydrogen
Struvite
Mg
316SS
NH4+
HnPO4n-3
Mg2+
H+
Anode
Cathode